



Technical Note

Characteristics of Rain-Induced Attenuation over Signal Links at Frequency Ranges of 25 and 38 GHz Observed in Beijing

Congzheng Han ^{1,2,*} , Liang Feng ^{2,3} , Juan Huo ^{1,2} , Zhaoze Deng ^{1,2} , Gaoyuan Zhang ^{1,4}, Baofeng Ji ^{1,4}, Yushu Zhou ^{2,3}, Yongheng Bi ^{1,2}, Shu Duan ^{1,2} and Renmin Yuan ⁵

¹ Key Laboratory for Middle Atmosphere and Global Environment Observation (LAGEO), Institute of Atmospheric Physics, Chinese Academy of Sciences, Beijing 100029, China; huojuan@mail.iap.ac.cn (J.H.); dengzz@mail.iap.ac.cn (Z.D.); 9905530@haust.edu.cn (G.Z.); baofengji@haust.edu.cn (B.J.); byh@mail.iap.ac.cn (Y.B.); duanshu@mail.iap.ac.cn (S.D.)

² University of Chinese Academy of Sciences, Beijing 100049, China

³ Key Laboratory of Cloud-Precipitation Physics and Severe Storms (LACS), Institute of Atmospheric Physics, Chinese Academy of Sciences, Beijing 100029, China; fengl@mail.iap.ac.cn (L.F.); zys@mail.iap.ac.cn (Y.Z.)

⁴ College of Information Engineering, Henan University of Science and Technology, Luoyang 471023, China

⁵ School of Earth and Space Sciences, University of Science and Technology of China, Hefei 230026, China; rmyuan@ustc.edu.cn

* Correspondence: c.han@mail.iap.ac.cn



Citation: Han, C.; Feng, L.; Huo, J.; Deng, Z.; Zhang, G.; Ji, B.; Zhou, Y.; Bi, Y.; Duan, S.; Yuan, R.

Characteristics of Rain-Induced Attenuation over Signal Links at Frequency Ranges of 25 and 38 GHz Observed in Beijing. *Remote Sens.* **2021**, *13*, 2156. <https://doi.org/10.3390/rs13112156>

Academic Editor: Giorgio Baiamonte

Received: 20 April 2021

Accepted: 26 May 2021

Published: 31 May 2021

Publisher's Note: MDPI stays neutral with regard to jurisdictional claims in published maps and institutional affiliations.



Copyright: © 2021 by the authors. Licensee MDPI, Basel, Switzerland. This article is an open access article distributed under the terms and conditions of the Creative Commons Attribution (CC BY) license (<https://creativecommons.org/licenses/by/4.0/>).

Abstract: Wireless communication has become a very important part of our lives, and it is well known that meteorological factors affect the quality of communication links, especially at higher frequencies because the physical dimensions of raindrops, hail stones, and snowflakes are on a similar wavelength to the propagating radio frequency. Millimeter-waves are an important technology for fifth-generation cellular networks which are currently being deployed all over the world. Since atmospheric effects are challenging in millimeter-wave transmissions, in this paper, we conducted line-of-sight field measurements at 25 GHz and 38 GHz. We monitored the received signal during rainfall events and compared the theoretical attenuation and the recorded rain-induced attenuation. We also derived the rain-induced attenuation (A) and rainfall rate (R) relation for stratiform and convective rain, respectively, using local rain drop size distribution (DSD) information at our measurement site collected during the period of two years. Furthermore, opportunistic sensing of atmospheric phenomena using microwave or millimeter-wave communication links in commercial cellular networks has recently attracted more attention in meteorological research worldwide. The accuracy of calculating rainfall rates from microwave links highly depends on the retrieval model and values of coefficients in the model, i.e., a and b of the A - R relation model. Here, the coefficients a and b are estimated based on local DSD measurement, and the performance of the improved A - R model is evaluated using propagated signal power based on measurement data. Compared to the (a , b) coefficients in the International Telecommunication Union Recommendation (ITU-R) P.838 document, the derived coefficients achieved an improved rainfall rate estimation.

Keywords: raindrop size distribution (DSD); microwave links; millimeter-wave link; 5G; radio propagation meteorological factors; rain-induced attenuation

1. Introduction

The fifth-generation cellular networks (5G) have been rapidly deployed worldwide, and millimeter-wave communication is one of its key enabling technologies. Millimeter-wave has a great advantage in high-capacity and high-speed communication due to its large available bandwidth [1–3]. Data rates in microwave frequencies and below are limited to about 1 Gb/s, but they can reach 10 Gb/s and more in the millimeter-wave range. The World Radiocommunication Conference (WRC) 2019 identified 24.25–27.5 GHz, 37–43.5 GHz, 45.5–47 GHz, 47.2–48.2 GHz, and 66–71 GHz for terrestrial systems that

deliver high-throughput, low-latency 5G services [4]. However, it is well known that electromagnetic signals may experience atmospheric loss as a result of oxygen, water vapor, rain, fog, snow, etc. [5]. Particularly, rain attenuation is less noticeable for lower frequency bands, but it can become more significant at frequencies greater than 10 GHz, as illustrated in Figure 1. The understanding of rain-induced signal attenuation is very important for the design of millimeter-wave radio communication systems.

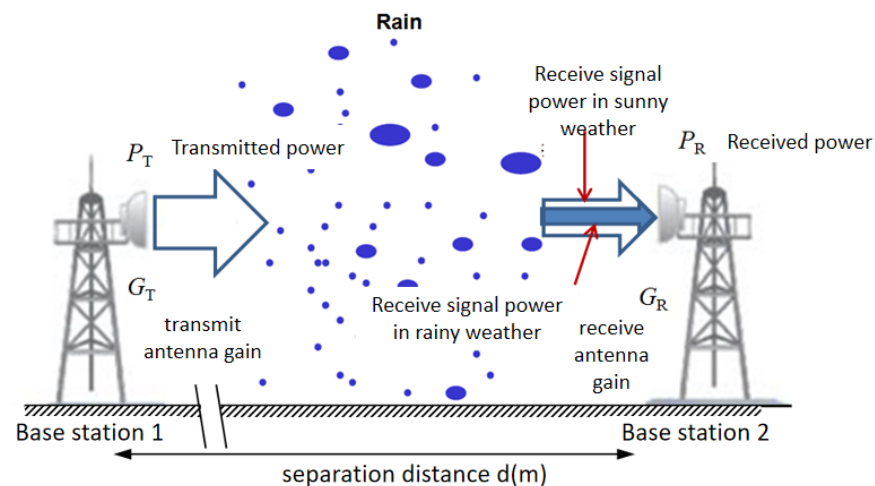


Figure 1. Schematic view of a wireless transmission link from one base station to another during rain and the received signal power is additionally attenuated by A (dB).

Regarding our study, we have built a 25 GHz and 38 GHz measurement link for understanding the impact of rainfall. Atlas et al. [6] already proved in 1977 that rain-induced microwave attenuation and a rainfall rate are nearly linearly related near wavelengths of 1 cm. A simple power law empirical model, which is expressed as $A = aR^b$, often is used for relating the rainfall rate (R) and the rain-induced attenuation (A) [7,8]. One of the most commonly used A - R relations with coefficients a and b at different frequencies is documented in the ITU [9], and the same coefficients are used all over the world. Different regions experience various rainfall patterns at different times of the year. Therefore, the information of raindrop size distribution is essential for formulating the local A - R relation. We have collected rain drop size distributions and rainfall rate statistics with a 1-min resolution, including the rainy season in Beijing (mainly from July to August [10] in 2017 and 2018), together with the 25 GHz and 38 GHz link measurements at our measurement site at the Institute of Atmospheric Physics (IAP), Chinese Academy of Science (CAS). We first analyze the rainfall behaviour based on these two years of raindrop size distribution measurement data. The average DSD for different precipitation types is studied. The coefficients (a , b) of the power law model are derived, aimed at providing a better prediction of rainfall affecting near-ground communication links at the measurement site. We then compare the theoretical rain-induced attenuation and recorded signal attenuation from our trial measurements.

Although attenuation caused by rainfall and other meteorological phenomena is undesired for commercial communication links, opportunistic sensing of rain using microwave links has been proven to be a promising new method for near-ground rainfall monitoring as a new remote sensing technology [11–14]. Most of the existing papers have adopted the $R = \sqrt[b]{A/a}$ relation which is derived from the ITU-R P. 838-3. The coefficients (a , b) depend on the local raindrop size distribution and rainfall characteristics, and they may vary in different regions. They affect the accuracy of rainfall rate estimation and the ITU model is not guaranteed to provide the best approximation of the relation between the rain-induced attenuation and the rainfall rate for a specific measurement. Therefore, microwave link-based rainfall monitoring research and applications also will benefit from locally-derived a and b values for the rainfall retrieval model. Furthermore, it is important

to associate rainfall with rainfall type in remote sensing and modeling studies [15]. We study the variation of coefficients (a , b) derived from different types of rainfall events. We then apply our derived coefficients for rainfall rate estimation and examine the accuracy of the modified model.

The main contribution of the paper is: (1) derivation of the rainfall rate and rainfall-induced attenuation power law relation based on local raindrop size distribution statistics recorded by a disdrometer during two years of measurement in Beijing, China; (2) analysis of rainfall-induced attenuation impairing the near-ground communication links, especially at millimeter-wave frequency ranges, using measurement data; (3) derivation of the coefficients of the model for rainfall rate retrievals using, local microwave link measurements, which are considered an emerging new technology for environmental monitoring, and sustainable sources of near-ground environmental data.

The structure of the paper has been organized as follows. The statistics of the average raindrop size distribution of convective and stratiform rain from two years of measurement data are discussed in Section 2. The relationship of the rainfall rate and the rain-induced attenuation based on measured data is examined and compared with the ITU-R P. 838-3 model, and the power law coefficients a and b , which have been derived locally, are examined for the use of retrieving the rainfall rate over a 25 GHz signal link in Section 3, while Section 4 draws the conclusions.

2. Materials and Methods

2.1. Rainfall Measurement Equipment

The rain measurements were recorded simultaneously by a rain gauge and an OTT Parsivel² [16] precipitation particle disdrometer. A disdrometer is a designated measuring device which can be used to monitor the type of the fallen precipitation, the precipitation rate, and the velocity and diameter of the fallen particles. It also can identify the type of precipitation (snow, sleet, rain, hail, etc.) and output the corresponding precipitation code [17]. The data from a disdrometer are well known for their use in studying the microphysical features of DSD for different rain types and climatic regimes [18–21]. Using post-processing of the measurement data, the rain DSD can be derived and the rain-induced attenuation can be calculated. Particles which are in diameters between 0.125–25 mm and in fall velocities between 0.1–22.4 ms⁻¹ are detectable by a disdrometer. There are 32 bin sizes for particle diameter and velocity, respectively, as detailed in [22,23]. The disdrometer and rain gauge were deployed on the roof top of Building 40 (39°59′03″ N, 116°23′38″ E) of IAP, CAS in Beijing, which sits along the northwest edge of the North China Plain.

2.2. Particle Size Distribution and Rainfall Rate

The number density of particles was calculated by the number of particles passing through the sensing surface of the Parsivel disdrometer within a given time interval [24,25] per-unit-of-volume per-unit-of-size interval:

$$N(D_i) = \sum_{j=1}^{32} \frac{C_{ij}}{v_j \times S \times T \times \Delta D_i} \left[\text{m}^{-3} \cdot \text{mm}^{-1} \right] \quad (1)$$

where C_{ij} represents the number of rain drops present at the i th diameter class and j th velocity class. $N(D_i)$ ($\text{m}^{-3} \cdot \text{mm}^{-1}$) is the concentration of raindrops per unit volume in the interval from D_i to $(D_i + \Delta D_i)$. D_i is the diameter of the rain drops in class i . S is 0.0052 m² which represents the sampling area of the disdrometer surface. T is the sampling interval of 60 s. ΔD_i is defined as the diameter interval between two consecutive classes ($i - 1$) and i . v_j is the particle fall speed in the j th velocity class. Once the particle size distributions

(PSDs) are calculated using the rain DSD measurements, the rainfall parameters of interest can be derived [26]:

$$R = 6\pi \times 10^{-4} \sum_{i=1}^{32} \sum_{j=1}^{32} v_j \times D_i^3 \times N(D_i) \Delta D_i \text{ [mm/h]} \quad (2)$$

The result for Equation (2) gives the estimated rainfall rate.

Rain DSD information affects the transmission performance of electromagnetic signals in the rain and is important for the prediction of the microwave signal attenuation due to rainfall. Analysis and modeling of the distribution of raindrops or drizzle has been extensively studied [27–29]. There are various models that have been applied for modeling rain DSD, such as the Marshall Palmer (M-P), exponential, lognormal, gamma distribution, Weibull, and Laws and Parsons [30–32] models. The exponential distribution for raindrop spectra proposed by Marshall and Palmer is in the following form [30]:

$$N(D) = N_0 \exp(-\Lambda D) \text{ [m}^{-3} \cdot \text{mm}^{-1}] \quad (3)$$

where $N(D)$ represents the rain DSD, N_0 is a constant in m^{-3} , $\Lambda(\text{mm}^{-1})$ is the slope parameter, and D (mm) is the equivalent volume diameter. Atlas and Ulbrich [32] suggested fitting a gamma function to the rain DSD, and the gamma distribution is widely used for representing natural DSD variability [33] in the form:

$$N(D) = N_0 D^\mu \exp(-\Lambda D) \text{ [m}^{-3} \cdot \text{mm}^{-1}] \quad (4)$$

where $N_0(\text{mm}^{-\mu-1} \cdot \text{m}^{-3})$ is the number concentration parameters, μ is the distribution shape parameter, $\Lambda(\text{mm}^{-1})$ is the slope parameter, and D (mm) is the equivalent volume diameter. It is generally accepted that the size distribution of droplets in rain of varying intensity follows the M-P distribution; the number of droplets distributed in the initial stage of rain (drizzle) is described by the gamma distribution function.

2.3. Outdoor Field Millimeter-Wave Measurement

Atmospheric attenuation due to rain can become more severe at millimeter frequencies. To gain an understanding of the relationship between the rainfall rate and rain-induced attenuation at our measurement site, we built line-of-sight transmission links of 80 m and 700 m long, and the operating frequency of the link was at 25 GHz or 38 GHz. Our field measurement started in 2016 and took place at IAP, CAS in central Beijing [34,35], as shown in Figure 2. Occurring at the transmitting end, we generated stable signals using a signal generator with negligible temperature-induced variations. The signal was then put through a horn antenna which was vertically polarized. Occurring at the receiver side, an identical horn antenna was connected to a signal analyzer for signal reception and display. The instantaneous received signal power was recorded. The measurement link setup and parameters are given in Table 1.

2.4. Estimation of Rain-Induced Attenuation Over Millimeter-Wave Links

Section 2.3 introduced our measurement campaign to monitor the rain-induced attenuation over millimeter-wave links. When measurement data are unavailable, two other ways to estimate the rain-induced attenuation are either through using available rain DSD data or using an ITU model if only the rainfall rate is available. Similar to the power law relationship of a Z-R model, which relates the radar reflectivity (Z) and rainfall rate (R) [36–38], the relationship between the rainfall rate (R) and attenuation (A) also is expressed by the A-R relation.

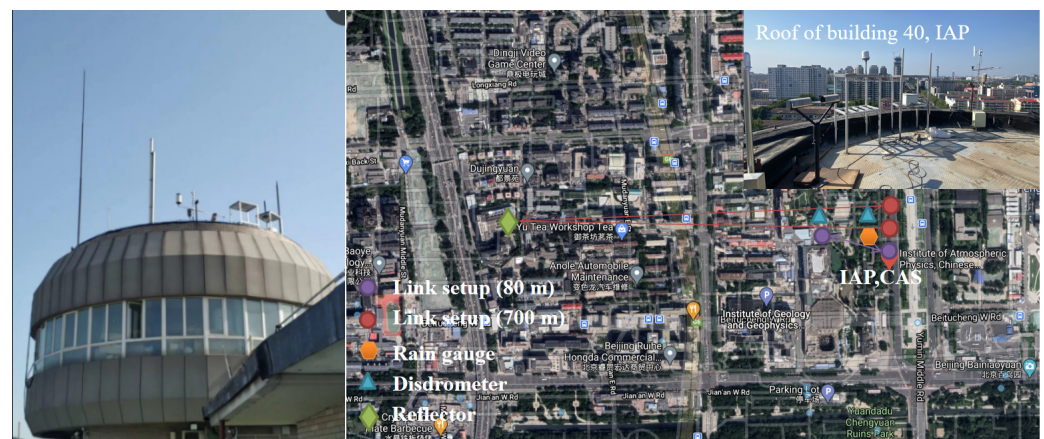


Figure 2. The transmission link and rain measurement setup.

Table 1. The outdoor field millimeter-wave link measurement setup.

Parameter	Value
Centre frequency	25 GHz/38 GHz
Transmit power	7 dBm
Transmitter instrument	Anritsu MG369XB signal generator
Receiver instrument	Agilent N9030A PXA signal analyzer
Antenna type	Horn antenna
Transmitter-Receiver (Tx-Rx) distance	80 m/700 m
Sampling interval	15 s
Tx antenna gain	23.8 dBi (25 GHz)/25.6 dBi (38 GHz)
Rx antenna gain	23.8 dBi (25 GHz)/25.6 dBi (38 GHz)
Polarization	Vertically polarized
Cable loss	2 m (−2.2 dB), 3 m (−5.0 dB)
Tx and Rx azimuth half-power beamwidth	11° (25 GHz)/8.4° (38 GHz)
Tx and Rx elevation half-power beamwidth	10° (25 GHz)/7.4° (38 GHz)

Due to its simplicity, a power law empirical model often is used in the calculation of rain-induced attenuation A and the rainfall rate R :

$$A = aR^b \text{ [dB/km]} \quad (5)$$

where the power law coefficients a and b are related to the polarization, frequency, and characteristics of the rain DSD. When the information for the rain DSD is not available, we can use existing models for the rainfall rate and rain-induced attenuation estimation. The ITU-R P.838-3 document gives a and b values for specific frequencies. These values are empirically calculated and the same values are used worldwide [9]. However, those coefficients depend on the local climate characteristics, rain types and, in fact, they are not the same from region to region.

Alternatively, we can derive a and b using the local rain by relating the rainfall rate and attenuation (A) as follows. Using the availability of the rainfall parameters, including the raindrop size distribution measurement from a local disdrometer, we can estimate the PSD based on Equation (1) and the rain-induced attenuation (A) by an integral of all the water drop sizes [39–41]:

$$A = 4.343 \times 10^{-3} \sum_i^{32} Q_{ext}(D_i, \lambda, m) N(D_i) \Delta D_i \text{ [dB/km]} \quad (6)$$

where Q_{ext} represents the attenuation cross section, which is dependent on the wavelength of the signal λ , the drop diameter D_i , and the water drop complex refractive index m . The water drop complex refractive index is a function of the frequency and the temperature.

Q_{ext} is estimated by applying the Mie scattering calculations for plane wave radiation to an absorbing sphere particle. Mie scattering considers the frequency and temperature properties of rain attenuation, but it does not consider the polarization and angular dependencies. It assumes that rain drop shape is spherical. $N(D_i)$ is the PSD, as presented in Equation (1). We can use Equation (5) to relate the rainfall rate measured by the disdrometer and the rain-induced attenuation calculated by Equation (6), and calculate the local coefficient values (a, b) . Since the A - R relation is modeled as a power law function, and the coefficient a is greater than 0, we can take logarithms from both sides of the Equations:

$$\begin{aligned} \lg(A) &= \lg(a) + b(\lg(R)) \\ Y &= \hat{a} + \hat{b}X \end{aligned} \quad (7)$$

where $Y = \lg(A)$, $X = \lg(R)$, $\hat{a} = \lg(a)$ and $\hat{b} = b$. Assuming there are N measurements, $(X_1, Y_1), (X_2, Y_2), \dots, (X_N, Y_N)$, the non-linear least square estimation method can be applied to find the line of best fit for the data sets, so (\hat{a}, \hat{b}) can be solved using the following Equations:

$$\begin{aligned} \hat{a} &= (\bar{Y} - \hat{b}\bar{X}) \\ \hat{b} &= \frac{\sum_{n=1}^N (X_n - \bar{X})(Y_n - \bar{Y})}{\sum_{n=1}^N (X_n - \bar{X})^2} \end{aligned} \quad (8)$$

where \bar{X} and \bar{Y} are the mean values. Once (\hat{a}, \hat{b}) are estimated, the power law coefficients (a, b) , based on local rain DSD data, can be derived.

2.5. Estimation of Rainfall Rate Using Millimeter-Wave Link

Although the large atmospheric attenuation of electromagnetic signals at millimeter-wave frequencies is undesirable for cellular networks, it has been proven to be an effective tool for weather estimation. Since first proposed in 2006 [11], and after more than a decade of world-wide research efforts, using commercial microwave or mmWave communication links for opportunistic sensing of atmospheric phenomena has become a well-established field [12,13]. Every link can be considered a virtual rain sensor, and the path-averaged rainfall rate can be retrieved from the link measurement. We will use the power law model as stated in Equation (5) to relate the attenuation to the rainfall rate:

$$R = \sqrt[b]{\frac{A}{aL}} \text{ (mm/h)} \quad (9)$$

Therefore, the average rainfall rate along a link can be derived from the microwave link rain-induced attenuation. The information about how to post-process measurement data can be found in [2,14]. When the local rain DSD data are available, alternatively, the values of a and b also can be derived using DSD information from local measurements, as discussed in Section 2.4.

3. Results and Discussion

3.1. Rainfall Statistics

The disdrometer data used in this study was collected mainly during the summer in both 2017 and 2018. Note that we started millimeter-wave transmission link measurement since 2016, but the disdrometer data collected during summer in 2016 was very limited, so we did not include the rain DSD data from 2016 in our analysis of rainfall statistics. To ensure the measurement data quality and reduce the instrument observation error, a quality control procedure was applied to the measured raindrop spectrum data first [42,43]. The disdrometer data sets are summarized in Table 2. The following procedures were applied: The drop spectrum with the total number of observed particles less than 10 in a single spectrum (sampling period) were discarded; Only rainfall rates >0.1 mm/h were considered; The difference between the particle velocity and Atlas velocity [44] needed to

be between $\pm 50\%$; Particles with the smallest two positions (<0.25 mm) and particle sizes larger than 8 mm in each drop spectrum were discarded. A rain event was defined on the basis of one hour or a longer rain-free period between two consecutive rainy minutes [26]. Also, rain events that lasted less than 30 min were discarded to reduce statistical errors because most rain events are intermittent.

Table 2. Rain Record from June 2017 to August 2018.

Date (yyyy.mm.dd)	Rain Time (minutes)	Peak Rain Rate (mm/h)	Date (yyyy.mm.dd)	Rain Time (minutes)	Peak Rain Rate (mm/h)
2017.06.22	1111	17.9	2018.06.09	99	17.1
2017.06.23	522	129	2018.06.12	58	32.6
2017.08.02	260	27.3	2018.06.13	42	14.3
2017.08.03	65	20.8	2018.06.17	275	150.9
2017.08.09	31	1.0	2018.06.25	47	2.5
2017.08.11	77	53.3	2018.07.11	770	21.8
2017.08.12	234	123.5	2018.07.12	179	4.1
2017.08.13	112	20.1	2018.07.16	230	121.4
2017.08.18	153	87.4	2018.07.17	535	168.2
2017.08.19	132	7.1	2018.07.24	292	22.4
2017.08.22	577	40.5	2018.08.11	68	113.5
2017.08.23	413	153.4	2018.08.13	62	37.5
2017.10.09	861	11.0	2018.08.18	284	56.4
2018.06.07	62	2.1	2018.08.19	33	1.5

It is necessary to classify precipitation type. The DSD data set then was classified into two categories, convective and stratiform rainfall types. The classification of rain types in this study was mainly based on disdrometer data using the method described by Bringi et al. [45] and adopted in many studies [45,46]. Therefore, for at least 10 consecutive one-minute rain samples, if the average rainfall rate was >0.5 mm/h and the standard deviation was <1.5 mm/h, then the sample was classified as stratiform rain; if the average rainfall rate was >5 mm/h and the standard deviation was >1.5 mm/h, then it was classified as convective rain. Samples that belonged neither to stratiform nor convective were classified as mixed type, which is beyond the scope of this study and, therefore, excluded.

During the measurement time, after going through the data quality-control and the classification of rainfall type, the observed rainfall was 77% stratiform and 23% convective. To gain a better understanding of the characteristics of the local rainfall, all events per rainfall type were grouped together forming an averaged DSD for each drop diameter. Particle observations were fit using the M-P and gamma distribution models, and the composite raindrop spectra for convective and stratiform events are shown in Figure 3. The convective spectra are noticeably wider than the stratiform spectra with a higher raindrop number concentration at each diameter class, showing a much higher rainfall rate and attenuation for convective events than from stratiform events, according to Equations (2) and (6). Convective events had more raindrops in the higher diameters, in comparison to the stratiform events. Regarding convective rainfall events, the M-P formula shows a better fit for large raindrop sizes, but the difference between the M-P and gamma functions are not significant.

3.2. Rain-Induced Attenuation Over Millimeter-Wave Links and Power Law Coefficients Based on Local DSD Measurement

The rain DSD information is important for deriving the coefficients (a , b) in the power law equations for relating the rainfall rate to the rain-induced attenuation in a microwave link for local experiments. Based on the local rain DSD measurement at IAP, CAS, the average power law fit coefficient values a and b were obtained by relating the rainfall rate and attenuation during the entire measurement period, as indicated in Figure 4. The rain-induced attenuation was calculated using Equation (6) based on DSD measurements from precipitation originating from the two types of clouds—convective and stratiform. The rain-induced attenuation estimated using the power law coefficients from the ITU-R

P.838 are plotted in Figure 4. Each point is estimated based on the aggregated drops over a one-minute interval, monitored by the local disdrometer. The dashed red lines represent a fit of the *A-R* model derived using the measurement data as detailed in Section 3.1. The solid black lines were plotted using the model in the ITU-R P.838-3.

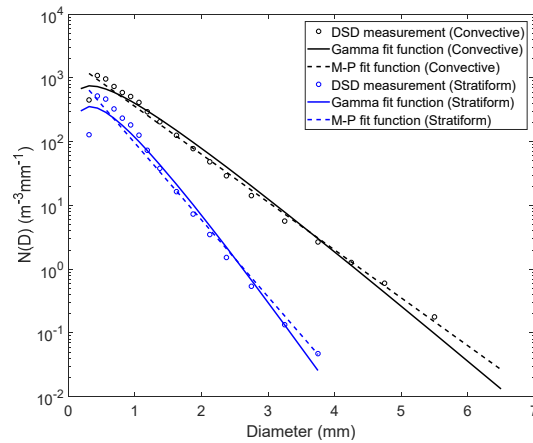


Figure 3. Composite raindrop spectra for convective and stratiform samples (circles). The gamma functions fitted on each spectrum using the non-linear least square estimation method (solid lines). The Marshall Palmer (M-P) functions fitted on each spectrum (dashed lines).

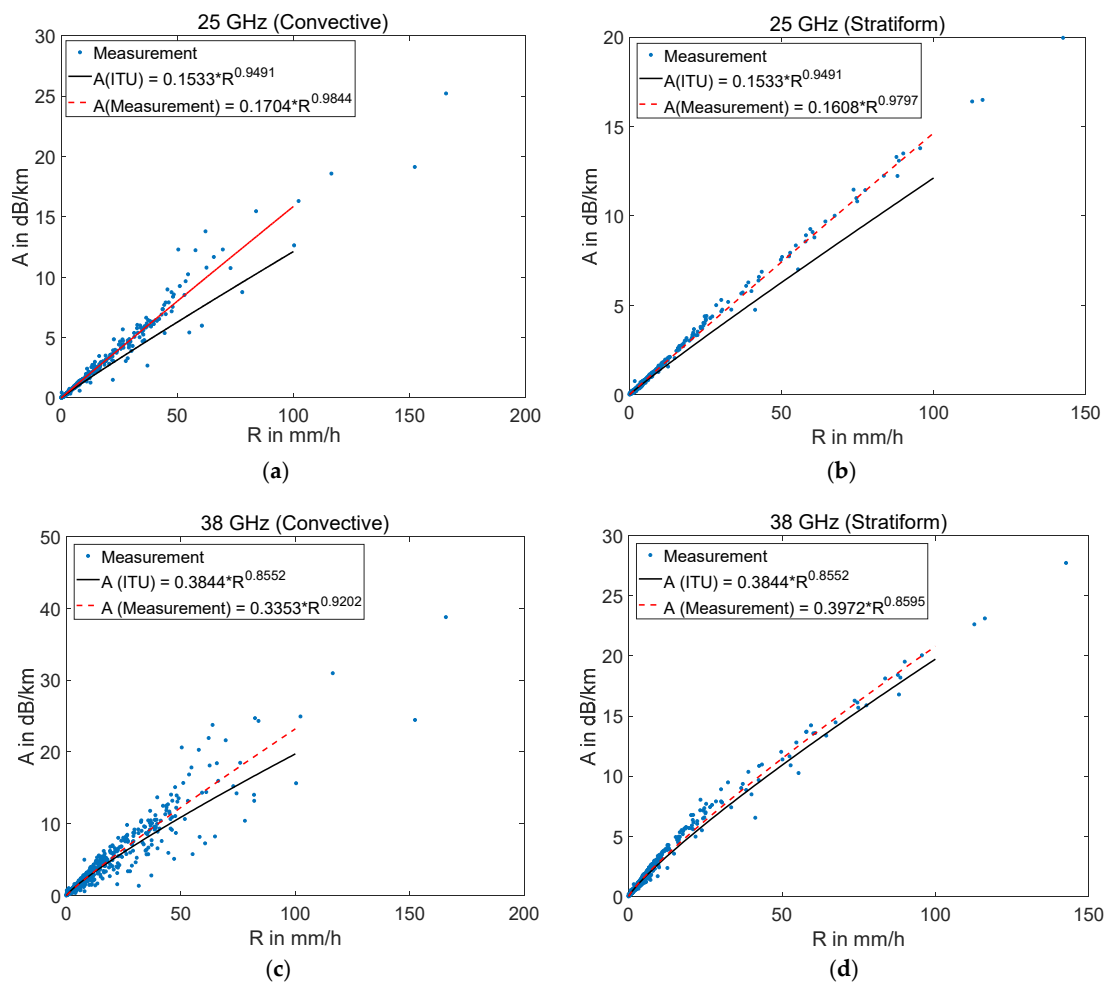


Figure 4. The relation between the rainfall rate *R* and attenuation *A* for (a) a 25 GHz link in convective precipitation (b) a 25 GHz link in stratiform precipitation (c) a 38 GHz link in convective precipitation (d) a 38 GHz link in stratiform precipitation.

Additionally, the a and b values also were derived on a daily basis when rainfall occurred for the convective and stratiform events, respectively. Figure 5 presents the a and b values for 16 stratiform rainfall events and six convective rainfall events compared to the values from the ITU-R P. 838 for 25 GHz and 38 GHz. Considering Figures 4 and 5, the derived a and b values based on measurement at IAP in Beijing are close to the values given in the ITU. While the rainfall rate increases, when the rainfall rate is greater than 10 mm/h, the rain-induced attenuation estimated by the ITU model is noticeably lower than the attenuation estimated by the local rain DSD information.

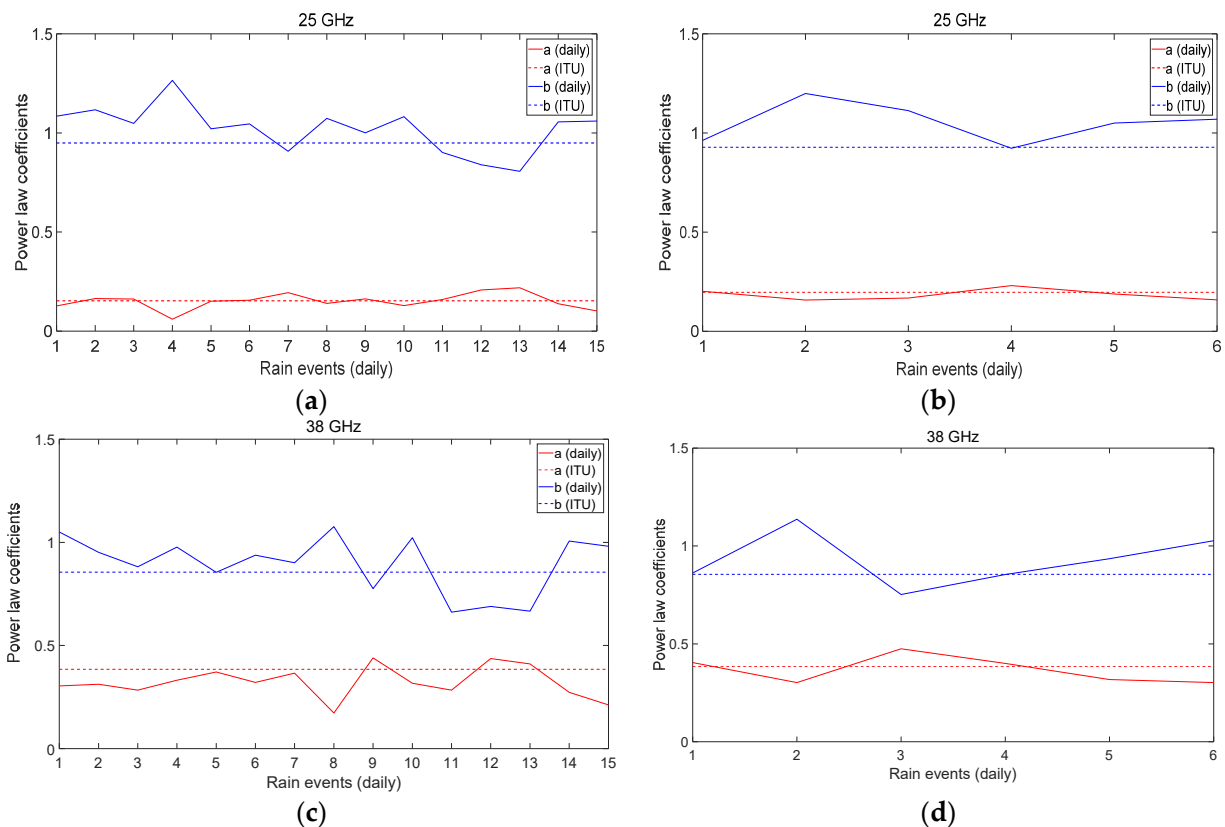


Figure 5. The comparison between power law coefficients (a , b) from the ITU-R P. 838-3 and the values derived from the measurement for (a) a 25 GHz link in stratiform precipitation (b) a 25 GHz link in convective precipitation (c) a 38 GHz link in stratiform precipitation (d) a 38 GHz link in convective precipitation.

3.3. Estimated Rainfall Rate Using Millimeter-Wave Link

Most of the existing rainfall rate retrieval studies are based on the power law model and coefficients given by the ITU-R document. Since climatic variations in different regions affect the rainfall characteristics, local information on raindrop size distributions has proven to be useful for formulating a more precise statistical prediction model for the local A - R relationship [47]. Therefore, it is necessary to conduct raindrop size distribution and millimeter-wave experiments to provide insightful information for research on the rainfall rate inversion of millimeter-wave links.

The performance of the improved A - R model is evaluated using propagated signal power based on measurement data in selected rainfall events as presented in Figure 6. The link-retrieved rainfall rate is evaluated based on the Pearson correlation coefficient and the mean relative error, and the formula is as follows:

$$r_k(X_{n,k}, Y_n) = \frac{1}{N-1} \sum_{n=1}^N \left(\frac{X_{n,k} - \mu_X}{\sigma_X} \right) \left(\frac{Y_n - \mu_Y}{\sigma_Y} \right) \quad (10)$$

$$MRE_k = \frac{100\%}{N} \times \sum_{n=1}^N \left| \frac{X_{n,k} - Y_n}{X_{n,k}} \right| \quad (11)$$

when k is 1, $X_{n,1}$ represents the rainfall rate (R_{ITU}) retrieved from the microwave link based on the power law coefficients from the ITU document, and when k is 2, $X_{n,2}$ represents the rainfall rate (R_{IAP}) retrieved from the microwave link based on our locally-derived coefficients at IAP, CAS in Beijing. Y_n represents the rainfall rate (R_{gauge}) measured by the local rain gauge, and is used as a reference data set. μ_X and σ_X are the mean and standard deviation of X_n , and μ_Y and σ_Y are the mean and standard deviation of Y_n , respectively. A higher correlation coefficient and lower mean relative error indicates the link-derived rainfall rate is more accurate compared to the ground truth data. It means that there is a better similarity between the two data sets, indicating that the rainfall rate estimation from the millimeter-wave link can represent the true rainfall rate well. Table 3 summarizes the rainfall rate correlation coefficient and mean relative error value from four selected days.

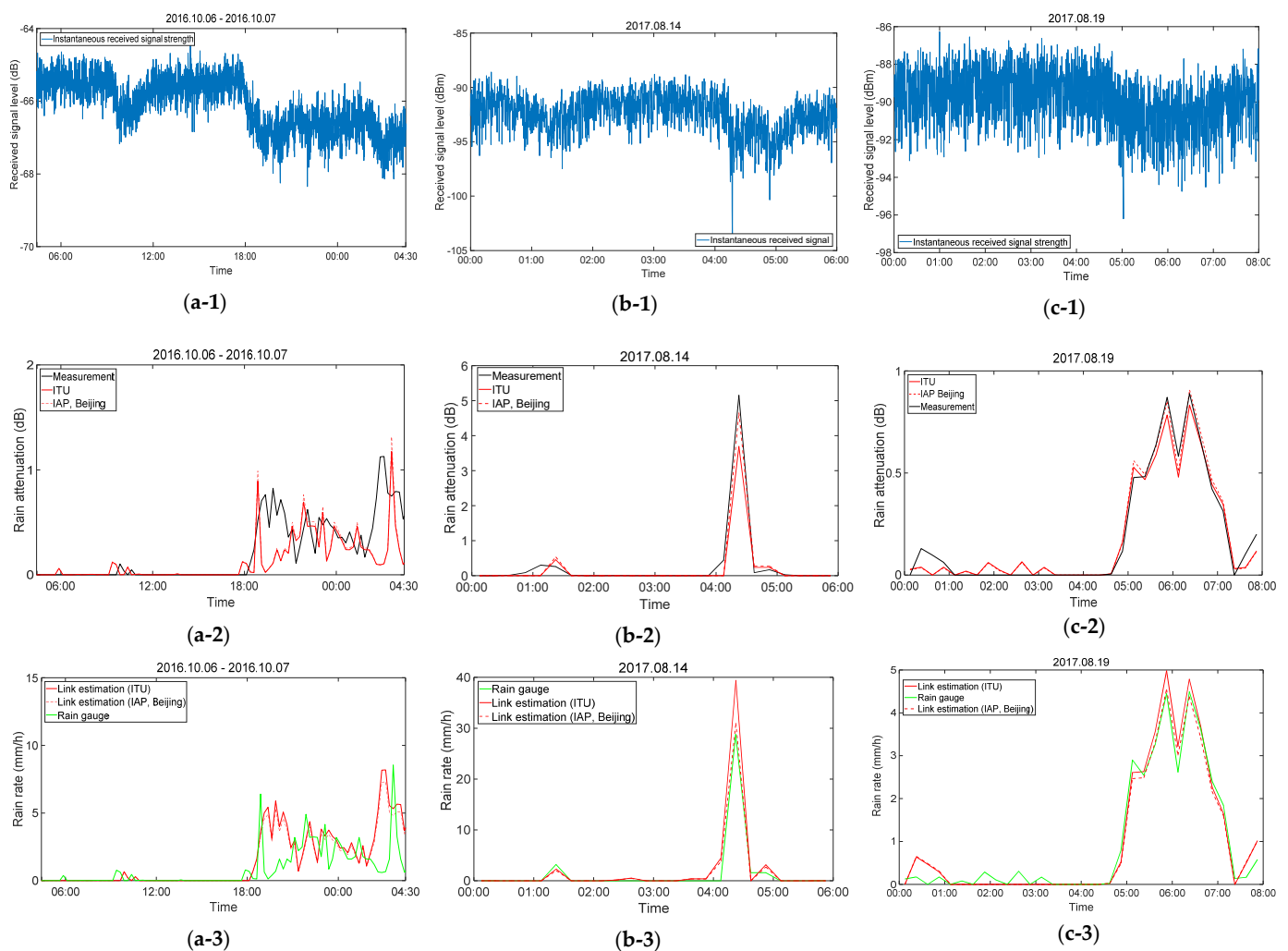


Figure 6. (a-1,b-1,c-1) Link instantaneous signal level on 6–7 October 2016, 14 August 2017, and 19 August 2017; (a-2,b-2,c-2) The measured average rain attenuation per 15 min, the rain attenuation based on the ITU model and rain attenuation calculated using locally derived coefficients on 6–7 October 2016, 14 August 2017, and 19 August 2017; (a-3,b-3,c-3) The link retrieved rainfall rate based on coefficients (a , b) from the ITU model and the derived (a , b) from local measurements, compared to the rain gauge measurement on 6–7 October 2016, 14 August 2017 and 19 August 2017. (Note the signal measurement is discussed in [48] but based on (a , b) coefficients in ITU-R P.838 document, the analysis in this paper shows the derived coefficients achieved an improved rainfall rate estimation).

Table 3. Correlation and mean relative error of the rainfall rate recorded by a rain gauge and estimated rainfall rate based on the power law coefficients from the ITU (R_{ITU}) or locally derived coefficients at IAP, CAS in Beijing (R_{IAP}).

Date (yyyy.mm.dd)	Frequency	R_{ITU}		R_{IAP}	
		$r_1(-)$	$MRE_1(\%)$	$r_2(-)$	$MRE_2(\%)$
2016.10.06–07	25 GHz	0.63	6.48	0.64	6.21
2017.08.14	25 GHz	0.98	0.54	0.98	0.38
2017.08.19	38 GHz	0.98	0.50	0.98	0.49

4. Discussion

The rainfall during 6 and 7 October 2016 was a stratiform rainfall event. The signal was transmitted over a short link of 80 m at a frequency of 25 GHz. Figure 6(a-1) shows the instantaneous received signal power. There was one recorded value of the received signal power per 15 s, and 60 recorded values within every 15-min interval. Shown in Figure 6(a-2,a-3), the calculated attenuation and retrieved rainfall rate using locally derived coefficients of (0.1608, 0.9797) gives some improved accuracy.

Regarding 14 August, 2017, Figure 6(b-1) shows 118 min of continuous rain data. Convective showers were dominant. The signal link was operated at 25 GHz, and the link length was approximately 700 m. The received signal experienced deep fade during this rainfall event. The measured rain-induced attenuation was averaged at a 15-min time interval and is presented in Figure 6(b-2). Using the power law coefficients given by the ITU and calculated from the local DSD, the estimated rain-induced attenuation also is compared in Figure 6(b-2). Figure 6(b-3) shows the rainfall rate derived using the signal link attenuation measurement. Overall, it shows that both the disdrometer-derived and ITU A - R model can provide a good estimate of the rainfall rate. When the average rainfall rate per 15 min exceeded 10 mm/h, the disdrometer-derived A - R model shows a noticeably better rainfall rate estimation. The peak rainfall rate was 28.8 mm/h, as recorded by the rain gauge at the roof of Building 40, IAP, CAS. The locally-derived A - R model gives a closer estimate of the peak rainfall rate of 31 mm/h, compared to the 39.4 mm/h estimated by the A - R model from the ITU. Note that the analysis considers a wet antenna attenuation of 3 dB during the rain.

The recordings of the received signal power on 19 August, 2017 are presented in Figure 6(c-1), and it was a stratiform rainfall event. The signal link was operated at 38 GHz, and the link length was approximately 700 m. Shown in Figure 6(c-2,c-3), the calculated attenuation and retrieved rainfall rate, using our derived local coefficients of (0.3972, 0.8589), shows improvement. The rainfall amount recorded by the rain gauge was 7.8 mm, and the rainfall amount estimated using the ITU model and locally-derived model were 8.2 mm and 7.7 mm, respectively.

The experimental results show that the accuracy of the rainfall rate retrieved from the microwave link data is relatively high. The mean relative errors are below 6.5%, and the correlation is above 0.6. Using locally calculated power law coefficients for the rainfall rate retrieval model provides some improvement in accuracy. Our measurement has a relatively short link distance compared to most commercial microwave links which are deployed over at least several kilometers [2]. Therefore, it is expected that the effectiveness of using local power law coefficients to improve the accuracy of the rainfall rate estimation will be more significant as the link length increases.

Previous studies have shown that accurate radar rainfall estimation with the Z - R model, which relates radar reflectivity (Z) and rainfall rate (R), relies heavily on the coefficients [49], and coefficients of the Z - R model can be very different for different rainfall events. To compare, the A - R model, which relates the rainfall-induced attenuation on the microwave signal link (A) and rainfall rate (R), our analyses show that the power law coefficients in the A - R relation do not change significantly for different rainfall events

compared to the Z - R relation. This also indicates that a microwave link provides a reliable and accurate near-ground rainfall estimation.

5. Conclusions

Atmospheric loss can be significant for wireless transmission, especially in the millimeter-frequency range. Existing studies on millimeter-wave channel measurements and modeling rarely consider the impact of changing atmospheric conditions. Here, we studied the impact of rainfall on 25 GHz and 38 GHz line-of-sight signal links. The rainfall rate and rain-induced attenuation model, based on local power law fit coefficients, were derived from two years of rainfall data recorded by a disdrometer at IAP, CAS in Beijing, China during 2017 and 2018. Preliminary analysis based on two years of raindrop size distribution information suggests that the power law coefficients from the ITU document give a reasonably good estimation of the rainfall rate and rain-induced attenuation at our experiment site. Several rainfall events were used for validation of the disdrometer-derived power law coefficients. The results show that the power law fit coefficients derived from local DSD data provide an improved accuracy for estimating rain-induced attenuation than the ITU model.

Opportunistic use of microwave links in the cellular network for environmental monitoring has been suggested as an Internet of Things (IoT) application. This technique was tested during this study using propagated signal power measurement data. The rainfall rate was retrieved using measured rain-induced attenuation based on the A - R relation. It was found that using the local disdrometer DSD data-derived power law coefficients for rainfall rate retrieval gives an improved estimation result, and this improvement is more noticeable for an increasing rainfall rate, compared to the case of using the power law coefficients from the ITU. Next, long-term observations of rainfall and drop size distribution parameters over longer deployment distances and at more measurement sites will be needed to produce accurate statistics of the rainfall for a region of interest. Longer observations also will provide more robust coefficients for the estimation of rain-induced attenuation and for the rainfall rate power law relation for different precipitation types. It also is important to consider the rainfall effects for millimeter-wave channel modeling, thus we will continue measurements at other frequencies and link lengths to improve our developed models.

Author Contributions: Conceptualization, C.H., J.H., G.Z., B.J., Y.B., S.D.; methodology, C.H., J.H., Z.D., L.F., Y.Z., R.Y.; software, J.H., S.D., C.H., G.Z. and B.J.; validation, C.H., J.H., Z.D., L.F., Y.Z., and R.Y.; formal analysis, C.H., L.F.; investigation, C.H., G.Z., B.J., R.Y.; resources, B.J., S.D., R.Y.; data curation, C.H., B.J., J.H.; writing—original draft preparation, C.H.; writing—review and editing, J.H., Z.D., L.F., G.Z., B.J., Y.Z., Y.B., S.D., R.Y.; visualization, C.H., L.F., Z.D.; supervision, C.H.; project administration, C.H., S.D.; funding acquisition, C.H.; All authors have read and agreed to the published version of the manuscript.

Funding: This research was funded by National Natural Science Foundation of China, grant number 41605122, 42027803, 41775032, 61701172, 61801170; LAGEO of Institute of Atmospheric Physics, Chinese Academy of Sciences (LAGEO-2019-2, LAGEO-2018-1); Young Backbone Teachers in Henan Province (2018GGJS049); Henan Province Young Talent Lift Project (2020HYTP009); Program for Science & Technology Innovation Talents in the University of Henan Province (20HASTIT022); China Postdoctoral Science Foundation (2018M633351).

Institutional Review Board Statement: Not applicable.

Informed Consent Statement: Not applicable.

Data Availability Statement: The data presented in this study are available on request from the corresponding author. The data are not publicly available due to restrictions privacy.

Conflicts of Interest: The authors declare no conflict of interest.

References

1. Daniels, R.C.; Heath, R.W.; Murdock, J.N.; Rappaport, T.S. *Millimeter Wave Wireless Communications*; Pearson: Upper Saddle River, NJ, USA, 2014; ISBN 978-0-13-217228-8.
2. Han, C.; Huo, J.; Gao, Q.; Su, G.; Wang, H. Rainfall monitoring based on next-generation millimeter-wave backhaul technologies in a dense urban environment. *Remote Sens.* **2020**, *12*, 1045. [CrossRef]
3. Zhang, G.; Han, C.; Ji, B.; Shi, C.; Xie, P.; Yang, L. A new multiple-symbol differential detection strategy for error-floor elimination of IEEE 802.15.4 BPSK receivers impaired by carrier frequency offset. *Wirel. Commun. Mob. Comput.* **2019**, *2019*, 1–26. [CrossRef]
4. Lin, T.; John, G. WRC-19 Revamps ITU Radio Regulations to Accommodate Emerging Communications Technologies. Available online: <https://www.hlregulation.com/2019/12/20/wrc-19-revamps-itu-radio-regulations-to-accommodate-emerging-communications-technologies/> (accessed on 20 December 2019).
5. Liebe, H.J.; Hufford, G.A.; Cotton, M.G. Propagation modeling of moist air and suspended water/ice particles at frequencies below 1000GHz, Electromagnetic Wave Propagation Panel Symposium. In Proceedings of the AGARD Conference Proceedings, Palma De Mallorca, Spain, 17–20 May 1993.
6. Atlas, D.; Ulbrich, C.W. Path- and area-integrated rainfall measurement by microwave attenuation in the 1–3 cm band. *J. Appl. Meteorol.* **1977**, *16*, 1322–1331. [CrossRef]
7. Medhurst, R.G. Rainfall attenuation of centimeter waves: Comparison of theory and measurement. *IEEE Trans. Antennas Propag.* **1965**, *13*, 550–564. [CrossRef]
8. Olsen, R.L.; Rogers, D.V.; Hodge, D.B. The aRb relation in calculation of rain attenuation. *IEEE Trans. Antennas Propag.* **1978**, *26*, 319–329. [CrossRef]
9. ITU-R P. 838-3 (International Telecommunication Union Radiocommunication Bureau Propagation Recommendation), Specific Attenuation Model for Rain for Use in Prediction Methods, 03/2005. Available online: <https://www.itu.int/rec/R-REC-P.838-3-200503-I/en> (accessed on 30 January 2021).
10. Wang, W.-C. Rainy Season at Beijing and Shanghai Since 1736. *J. Meteorol. Soc. Jpn.* **2008**, *86*, 827–834. [CrossRef]
11. Messer, H.; Zinevich, A.; Alpert, P. Environmental monitoring by wireless communication networks. *Science* **2006**, *312*, 713. [CrossRef]
12. Messer, H. Capitalizing on Cellular Technology—Opportunities and Challenges for Near Ground Weather Monitoring. *Environ. Sci. Technol.* **2018**, *5*, 73. [CrossRef]
13. Chwala, C.; Kunstmann, H. Commercial Microwave Link Networks for Rainfall Observation: Assessment of the Current Status and Future Challenges. *Wiley Interdiscip. Rev. Water* **2018**, *6*, 2018. [CrossRef]
14. Uijlenhoet, R.; Overeem, A.; Leijnse, H. Opportunistic remote sensing of rainfall using microwave links from cellular communication networks. *Wiley Interdiscip. Rev. Water* **2018**, *5*, e1289. [CrossRef]
15. Tokay, A.; Short, D.A. Evidence from tropical raindrop spectra of the origin of rain from stratiform versus convective clouds. *J. Appl. Meteorol.* **1996**, *35*, 355–371. [CrossRef]
16. Available online: <https://www.ott.com/products/meteorological-sensors-26/ott-parsivel2-laser-weather-sensor-2392/> (accessed on 30 January 2021).
17. Park, S.G.; Kim, H.L.; Ham, Y.W.; Jung, S.H. Comparative Evaluation of the OTT PARSIVEL2 Using a Collocated Two-Dimensional Video Disdrometer. *J. Atmos. Ocean. Technol.* **2017**, *34*, 2059–2082. [CrossRef]
18. Atlas, D.; Ulbrich, C.W.; Marks, F.D., Jr.; Black, R.A.; Amitai, E.; Willis, P.T.; Samsury, C.E. Partitioning tropical oceanic and stratiform rains by draft strength. *J. Geophys. Res.* **2020**, *105*, 2259–2267. [CrossRef]
19. Atlas, D.; Ulbrich, C.W. Drop size spectra and integral remote sensing parameters in the transition from convective to stratiform rain. *Geophys. Res. Lett.* **2006**, *33*, L16803. [CrossRef]
20. Tokay, A. Comparison of drop size distribution measurements by impact and optical disdrometers. *J. Appl. Meteorol.* **2001**, *40*, 2083–2097. [CrossRef]
21. Wu, Z.; Zhang, Y.; Zhang, L.; Lei, H.; Xie, Y.; Wen, L.; Yang, J. Characteristics of summer season raindrop size distribution in three typical regions of western pacific. *Geophys. Res. Atmos.* **2019**, *124*, 4054–4073. [CrossRef]
22. Wen, G.; Xiao, H.; Yang, H.; Bi, Y.; Xu, W. Characteristics of summer and winter precipitation over northern China. *Atmos. Res.* **2017**, *197*, 390–406. [CrossRef]
23. Tang, Q.; Xiao, H.; Guo, C.; Feng, L. Characteristics of raindrop size distributions and their retrieved polarimetric radar parameters in northern and southern China. *Atmos. Res.* **2014**, *135–136*, 59–75. [CrossRef]
24. Chen, B.; Hu, W.; Pu, J. Characteristics of the raindrop size distribution for freezing precipitation observed in southern China. *J. Geophys. Res. Space Phys.* **2011**, *116*, D06201. [CrossRef]
25. Raupach, T.H.; Berne, A. Correction of raindrop size distributions measured by Parsivel disdrometers, using a two-dimensional video disdrometer as a reference. *Atmos. Meas. Tech.* **2014**, *7*, 8521–8579. [CrossRef]
26. Fielding, M.D.; Chiu, J.C.; Hogan, R.J.; Feingold, G.; Eloranta, E.; O’Connor, E.J.; Cadeddu, M.P. Joint retrievals of cloud and drizzle in marine boundary layer clouds using ground-based radar, lidar and zenith radiances. *Meas. Tech. Discuss.* **2015**, *8*, 1833–1889.
27. Hugh, M.; Wojciech, G. Comparison of bulk and bin warm-rain microphysics models using a kinematic framework. *AMS J. Atmos. Sci.* **2007**, *64*, 2839–2861.

28. Miles, N.L.; Verlinde, J.; Clothiaux, E. Cloud droplet size distributions in low-level stratiform clouds. *J. Atmos. Sci. AMS* **2000**, *57*, 295–311. [[CrossRef](#)]
29. Marshall, J.S.; Palmer, W.M.K. The distribution of rain drops with size. *J. Meteorol.* **1945**, *5*, 165–166. [[CrossRef](#)]
30. Levin, L.M. The coagulation of charged cloud-droplets size distribution function for cloud droplets and rain drops. *Dokl. Akad. Nauk SSSR* **1954**, *94*, 1045–1053.
31. Ulbrich, C.W. Natural variations in the analytical form of the raindrop size distribution. *J. Appl. Meteorol.* **1983**, *22*, 1764–1775. [[CrossRef](#)]
32. Cao, Q.; Zhang, G.; Brandes, E.A.; Schuur, T.J. Polarimetric radar rain estimation through retrieval of drop size distribution using a bayesian approach. *J. Appl. Meteorol. Clim.* **2010**, *49*, 973–990. [[CrossRef](#)]
33. Huo, J.; Tian, Y.; Wu, X.; Han, C.; Liu, B.; Bi, Y.; Duan, S.; Lyu, D. Properties of ice cloud over Beijing from surface Ka-band radar observations during 2014–2017. *Atmos. Phys. Chem.* **2020**, *20*, 14377–14392. [[CrossRef](#)]
34. Huo, J.; Li, J.; Duan, M.; Lv, D.; Han, C.; Bi, Y. Measurement of cloud top height: Comparison of MODIS and ground-based millimeter radar. *Remote Sens.* **2020**, *12*, 1616. [[CrossRef](#)]
35. Matrosov, S.Y. Synergetic use of millimeter- and centimeter-wavelength radars for retrievals of cloud and rainfall parameters. *Atmos. Chem. Phys.* **2010**, *10*, 3321–3331.
36. Protat, A.; Klepp, C.; Louf, V.; Petersen, W.A.; Alexander, S.P.; Barros, A.; Leinonen, J.; Mace, G.G. The Latitudinal variability of oceanic rainfall properties and its implication for satellite retrievals: 2. The relationships between radar observables and drop size distribution parameters. *J. Geophys. Res. Atmos.* **2019**, *124*, 13312–13324. [[CrossRef](#)]
37. Zhou, L.; Dong, X.; Fu, Z.; Wang, B.; Leng, L.; Xi, B.; Cui, C. Vertical distribution of raindrops and Z-R relationships using microrain radar and 2-D video disdrometer measurements during the integrative monsoon frontal rainfall experiment (IMFRE). *J. Geophys. Res. Atmos.* **2020**, *125*, e2019JD031108. [[CrossRef](#)]
38. Lam, H.Y.; Luini, L.; Din, J.; Capsoni, C.; Panagopoulos, A.D. Investigation of rain attenuation in equatorial Kuala Lumpur. *IEEE Antennas Wirel. Propag. Lett.* **2012**, *11*, 1002–1005. [[CrossRef](#)]
39. Van Leth, T.C.; Overeem, A.; Leijnse, H.; Uijlenhoet, R. A measurement campaign to assess sources of error in microwave link rainfall estimation. *Atmos. Meas. Tech.* **2018**, *11*, 4645–4669. [[CrossRef](#)]
40. Leijnse, H.; Uijlenhoet, R. The effect of reported high-velocity small raindrops on inferred drop size distributions and derived power laws. *Atmos. Chem. Phys.* **2010**, *10*, 6807–6818. [[CrossRef](#)]
41. Murata, F.; Terao, T.; Chakravarty, K.; Syiemlieh, H.; Cajee, L. Characteristics of orographic rain drop-size distribution at Cherrapunji, Northeast India. *Atmosphere* **2020**, *11*, 777. [[CrossRef](#)]
42. Guyot, A.; Pudashine, J.; Protat, A.; Uijlenhoet, R.; Pauwels, V.R.N.; Seed, A.; Walker, J.P. Effect of disdrometer type on rain drop size distribution characterisation: A new dataset for south-eastern Australia. *Hydrol. Earth Syst. Sci.* **2019**, *23*, 4737–4761. [[CrossRef](#)]
43. Atlas, D.; Srivastava, R.C.; Sekhon, R.S. Doppler radar characteristics of precipitation at vertical incidence. *Rev. Geophys.* **1973**, *11*, 1–35. [[CrossRef](#)]
44. Chen, B.; Yang, J.; Pu, J. Statistical characteristics of raindrop size distribution in Meiyu season observed in Eastern China. *J. Meteorol. Soc. Jpn.* **2013**, *91*, 215–227. [[CrossRef](#)]
45. Bringi, V.N.; Chandrasekar, V.; Hubbert, J.; Gorgucci, E.; Randeu, W.L.; Schoenhuber, M. Raindrop size distribution in different climatic regimes from disdrometer and dual-polarized radar analysis. *J. Atmos. Sci.* **2003**, *60*, 354–365. [[CrossRef](#)]
46. Fu, Z.; Dong, X.; Zhou, L.; Cui, W.; Wang, J.; Wan, R. Statistical characteristics of raindrop size distributions and parameters in Central China during the Meiyu seasons. *J. Geophys. Res. Atmos.* **2020**, *125*, 1–15. [[CrossRef](#)]
47. Luini, L.; Roveda, G.; Zaffaroni, M.; Costa, M.; Riva, C.G. The impact of rain on short E-band radio links for 5G mobile systems: Experimental results and prediction models. *IEEE Trans. Antennas Propag.* **2020**, *68*, 3124–3134. [[CrossRef](#)]
48. Han, C.; Bi, Y.; Duan, S.; Lu, G. Rain rate retrieval test from 25 GHz, 28 GHz, and 38 GHz millimeter-wave link measurement in Beijing. *IEEE J. Sel. Top. Appl. Earth Obs. Remote Sens.* **2019**, *12*, 2835–2847. [[CrossRef](#)]
49. de Vos, L.W.; Raupach, T.H.; Leijnse, H.; Overeem, A.; Berne, A.; Uijlenhoet, R. High-resolution simulation study exploring the potential of radars, crowdsourced personal weather stations, and commercial microwave links to monitor small-scale urban rainfall. *Water Resour. Res.* **2018**, *54*, 10293–10312.